Nanoscale electron diffraction and plasmon spectroscopy of single- and few-layer boron nitride

C. T. Pan,[1,2] R. R. Nair,[1,*] U. Bangert,[2,*] Q. Ramasse,[3] R. Jalil,[1] R. Zan,[1] C. R. Seabourne,[4] and A. J. Scott[4]

[1]*School of Physics and Astronomy, The University of Manchester, Manchester M13 9PL, UK*

[2]*School of Materials, The University of Manchester, Manchester M13 9PL, UK*

[3] *SuperSTEM Laboratory, STFC Daresbury, Keckwick Lane, Daresbury WA4 4AD, UK*

[4]*Institute for Materials Research, SPEME, University of Leeds, Leeds LS2 9JT, UK*

(Received 12 August 2011; revised manuscript received 24 October 2011; published 24 January 2012)

Boron nitride (BN) sheets were exfoliated, and proof of the presence of single and double layers was obtained via electron diffraction and plasmon electron energy loss spectroscopy. A plasmon structure unique to mono- and bi-layer BN was established, and was accompanied by WIEN2K DFT calculations. The latter reproduced plasmon energies and general plasmon structure well; however, the detailed shape of the π-plasmon of the calculated pure BN spectra shows discrepancies with the experimental data. The theoretical models were then modified to include impurity atoms. Both oxygen and carbon impurities were considered, as well as different structures, including singular oxygen atoms and oxygen next to carbon atoms. These various configurations were obtained by analyzing atomic-resolution high-angle annular dark field (HAADF) images. Using these modified models, a π-plasmon structure close to the experimentally observed structure could be simulated.

PACS number(s): 68.37.Ma, 68.37.Lp, 61.48.De, 62.23.Kn

I. INTRODUCTION

Recent developments in graphene research have stimulated intense interest in the study of other two-dimensional materials such as boron nitride (BN), MoS$_2$, etc.[1–5] Unlike other layered materials, hexagonal boron nitride (hBN) is structurally similar to that of graphene but has complementary properties. It is a good insulator with a band gap of $\sim$5.9 eV.[6] Recent studies show that thin hBN is a prominent insulator for graphene-based electronic devices.[7,8] It is considered the thinnest possible insulator. Even though single-layer hBN has been isolated[1] and studied,[9,10] very little is known about its unique properties because of the difficulty in fabricating large single-layer hBN and the lack of characterization techniques able to distinguish single-layer BN from a few layers.[11] Earlier attempts to study single-layer BN were conducted on very small flakes prepared with an electron beam *in situ* within a transmission electron microscope (TEM)[9–12] or with reactive ion etching.[13] These techniques only provided nanometer-size BN sheets at the edges of thick BN with limited use for in-depth studies. However, with the progress in growing high-quality bulk hBN and mechanical exfoliation, it is now possible to obtain single-layer hBN with a large crystal size.[11] The single layer signature obtained from Raman and optical contrast analysis of large exfoliated BN sheets is weak compared with that from a few layers, unlike the case with graphene counterparts.[11] Only step height analysis with atomic force microscopy (AFM) provided evidence for the existence of single-layer BN. In this report, we use electron diffraction and electron energy loss spectroscopy (EELS) to characterize large, free-standing BN sheets. Both techniques can prove the existence of single layers; the latter technique, as in the case of graphene,[14] uses the unambiguous fingerprint of the π- and σ-plasmon to reveal not only the single layer nature, but also the occurrence of impurities, in BN because of their distinct effect on the plasmon structure. Density functional theory calculations have proven very useful in predicting and understanding the experimental plasmon spectra.

II. EXPERIMENTAL

Large single- and few-layer BN membranes were prepared by the method previously reported[15] for the fabrication of free-standing graphene. In brief, BN flakes were obtained by mechanical exfoliation[1] of high-quality hBN[6,16] on a Si/SiO$_2$ substrate, which allows easy preliminary characterization with optical techniques.[11] Single- and few-layer BN flakes were identified by optical contrast analysis and Raman spectroscopy.[11] To transfer these flakes to a TEM grid, we first spin-coated a thin (200 nm) poly(methyl methacrylate) (PMMA) layer on top. Later the BN-PMMA layers were released from the SiO$_2$ substrate by etching in a 3% KOH solution. After release, the BN flakes covered with PMMA were floated off in the KOH solution. Following ample rinsing with clean water, the BN-PMMA layer was transferred to a TEM grid (Quantifoil). Finally, we dissolved the PMMA using acetone, thus leaving the BN on a Quantifoil grid. The TEM grid covered with the BN flakes was dried in a critical-point dryer to prevent the membrane from rupturing because of surface tension.

Membranes obtained in this way were extremely stable and robust. Figure 1(a) shows a low-magnification TEM image of one of our single-layer membranes. The mechanical stability of this membrane, which is only supported on one side, demonstrates the high stiffness of single-layer BN, similar to that of graphene.[17] Figure 1(b) is a high-magnification TEM image of single-layer BN showing clean areas surrounded by hydrocarbon chains, which are also common to graphene membranes. The sizes of these clean areas in BN membranes are, however, larger than the typical sizes of clean regions in graphene membranes. This can be attributed to the less lipophilic nature of BN compared with graphene.

Structural screening and electron diffraction experiments were carried out in a Tecnai F30 TEM. Atomic lattice imaging in high-angle annular dark field (HAADF) mode and EELS measurements were carried out at the SuperSTEM facility (Daresbury, UK) on a Nion UltraSTEM scanning transmission
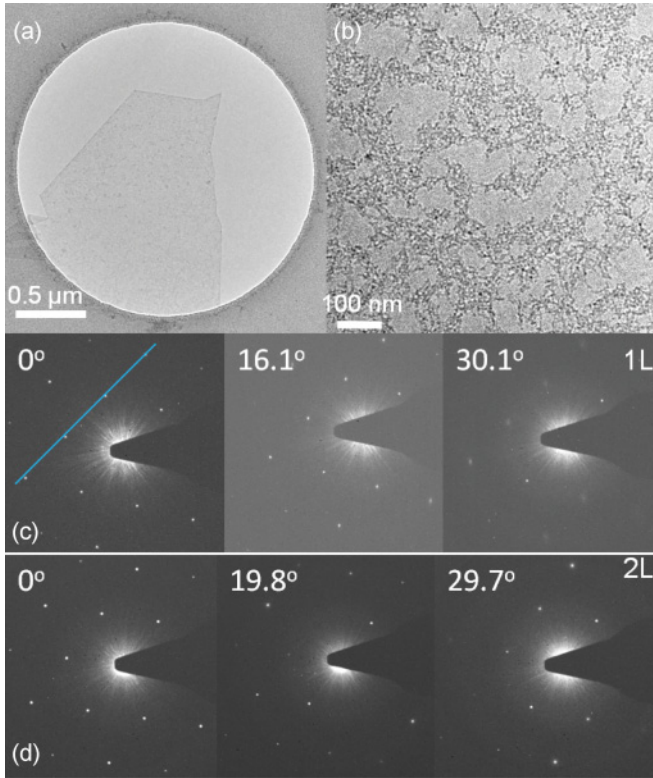
FIG. 1. (Color online) (a) Low-magnification electron micrograph of a single-layer BN flake freely suspended over a circular hole in a TEM grid; (b) part of the flake at larger magnification, showing clean areas—on the order of 100 nm—surrounded by macromolecular deposits; (c) diffraction patterns of the single-layer area (~0.3 μm in diameter) in panel b at various tilts (the blue diagonal line in the zero-tilt pattern is the line along which the intensity profile in Fig. 2(c) is taken); (d) diffraction patterns of double-layer area at various tilts.

electron microscope (STEM)[18] using a cold-field emission electron source and a corrector of third and fifth order aberrations. The STEM is also fitted with a Gatan Enfina EELS spectrometer. The probe size for HAADF imaging was ~1 Å and was similar for EEL spectrum image acquisition. Recording times for individual spectra, in most cases obtained with a 0.1-eV spectrometer dispersion, were on the order of 10^{-3} to 10^{-1} s, depending on the chosen pixel size; hence,

spectrum images (maps of EEL spectra acquired in each pixel of a predefined raster) of certain areas were obtained within times ranging from less than one minute to a few minutes. Damage to the BN layers (hole formation and peeling) mostly occurred in repeat scans of the same area.

III. DENSITY FUNCTIONAL THEORY CALCULATIONS

For plasmon calculations, WIEN2K was used. Throughout the calculations, the generalized gradient approximation (GGA) was used, in the Perdew–Burke–Enzerhof (PBE) 96 form.[19] The optic package within the code was employed.[20] Applications of the procedure are described in detail elsewhere.[21] The optimum conditions (number of k-points and RKmax) for the EELS calculations were found through convergence tests.[21–23] (A B-N bond length of 1.45 Å and a muffin tin radius of 1.36 Bohr for all atoms was used throughout.) To model two-dimensional (2D) structures of single- or double-layer BN, repeat structures of single and of double sheets (the latter with the bulk BN layer separation), respectively, were spaced at distances large enough (e.g., 60 Å) to prohibit interaction. To compare our simulations with the experimental spectra of 0.3-eV energy resolution, a Lorentzian broadening of 0.3 eV was imposed. Using the above parameters and setting the charge convergence criterion for the self-consistent cycles to 0.1, spectra of bulk, double-layer, and single-layer pure BN were calculated.

IV. RESULTS AND DISCUSSION

A. Diffraction patterns

Electron diffraction patterns of single- and double-layer BN are shown in Figs. 1(c) and 1(d), respectively. Changes of intensity and shape of the diffraction spots with tilt angle are also shown. Similar to graphene,[24] the diffraction pattern remains the same with tilting, which is indicative of a single layer; only at very high tilts (here ~30°) do the spots away from the tilt axis become blurred. In contrast, in the double layer, the spot pattern shows the changes in diffraction spot intensities expected from increasing Bragg restriction due to the emergence of lattice planes (note the disappearance of spots in the double layer at 19.8° tilt). The graphs in Figs. 2(a) and 2(b) show the dependence of the full width at half maximum (FWHM) and the intensity of the 0 −1 1 0 spot in single- and
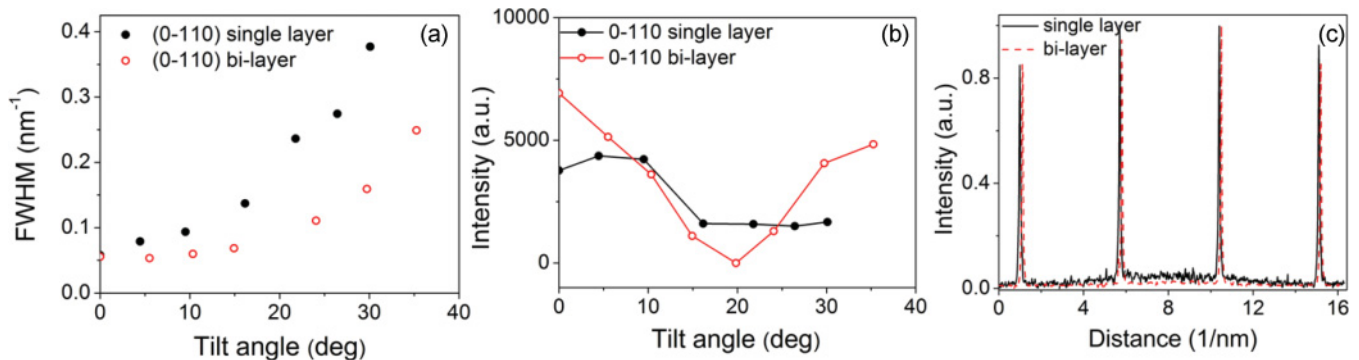

FIG. 2. (Color online) (a) Full width at half maximum (FWHM) and (b) intensity of the diffraction spots in single- and double-layer BN as a function of tilt angle; (c) intensity profile of diffraction spots in single- and double-layer BN plotted along the line in Fig. 1(c).

double-layer BN as a function of tilt angle. The increase of the FWHM with tilt angle indicates the rippling of the BN membrane in a way similar to graphene.[24] The total intensity of the diffraction spots for single-layer BN remains almost constant, whereas the double layer shows a distinct minimum in the intensity at 20° in Fig. 2(b). Figure 2(c) is the intensity profile along the line shown in Fig. 1(c) of BN at zero tilt. The single layer shows the familiar dome-shaped intensity profile of graphene;[25] the double layer shows the same profile. This is contrary to double-layer graphene, in which the outer spots are more intense than the inner spots because of the AB stacking of graphite; BN, however, is AA′ stacked, rendering the diffraction intensities of single and multiple layers at zero tilt similar.

B. Plasmon electron energy loss spectroscopy

DFT calculations of the dielectric function of bulk hBN have been presented by Arenal *et al.*[26] and of plasmons in single-wall BN nanotubes by Marinopolous *et al.*[27] The latter authors have also carried out calculations for flat, single-BN sheets, which show good agreement with WIEN2K calculations carried out in this paper. All calculations result in a π-plasmon, which is situated at ~6 eV and exhibits a slight shoulder at the rise [e.g., red curve; Fig. 3(b)] and a Lorentzian-shaped drop of its high-energy tail. The σ-plasmon has a sawtooth shape, peaking at ~14.3 eV, and the plasmons are similar in energy and appearance to those in graphene. Figure 3 shows that the agreement between WIEN2K calculations and

experimental low-loss spectra is good in terms of the energy loss peak positions, especially for the π-plasmon (at ~6.3 eV), and the general shape of the energy loss intensity distribution, although as a general trend, the experimental spectra are shifted upward in energy by a few tenths of an electron-volt, and the experimental data show a steeper rise, adding to the fact that the second peak at 7.5 eV is not reproduced in the calculation. In the literature, this second peak or high-energy shoulder in the π-plasmon was attributed to an interband transition, and a rigid shift of the energy positions;[26] this discrepancy was thought to have its origin in the deficiencies of the calculated dielectric constants. Furthermore, the enhancement of the peak at 7.5 eV in double layers suggests the contribution of a bulk-type effect, which the monolayer description does not account for, and it does not explain this feature in single layers. The authors in Ref. 26 show experimentally and theoretically for multiwall nanotubes, for which the ratio between inner and outer radii tends to 1, and also for single-wall nanotubes (SWNTs), that the polarizabilities are proportional to $\mathrm{Im}(-1/\varepsilon_\perp + \varepsilon_{||})$, where $\varepsilon_{||}$ and $\varepsilon_\perp$ are, respectively, the components of the dielectric tensor parallel and perpendicular to the BN sheet. Arenal *et al.*[26] remark further that the similarity between theoretical EELS and calculated curves reproduced the similarities observed between experimental EELS and measured $\varepsilon_{2||}$ curves in BN nanotubes, which implies that the contribution of the out-off-plane excitation remains quite small. On comparing experimental and calculated spectra in our results for single and bilayer BN, similarly, the out-of plane component appears to add little to the change in shape of the π-plasmon.
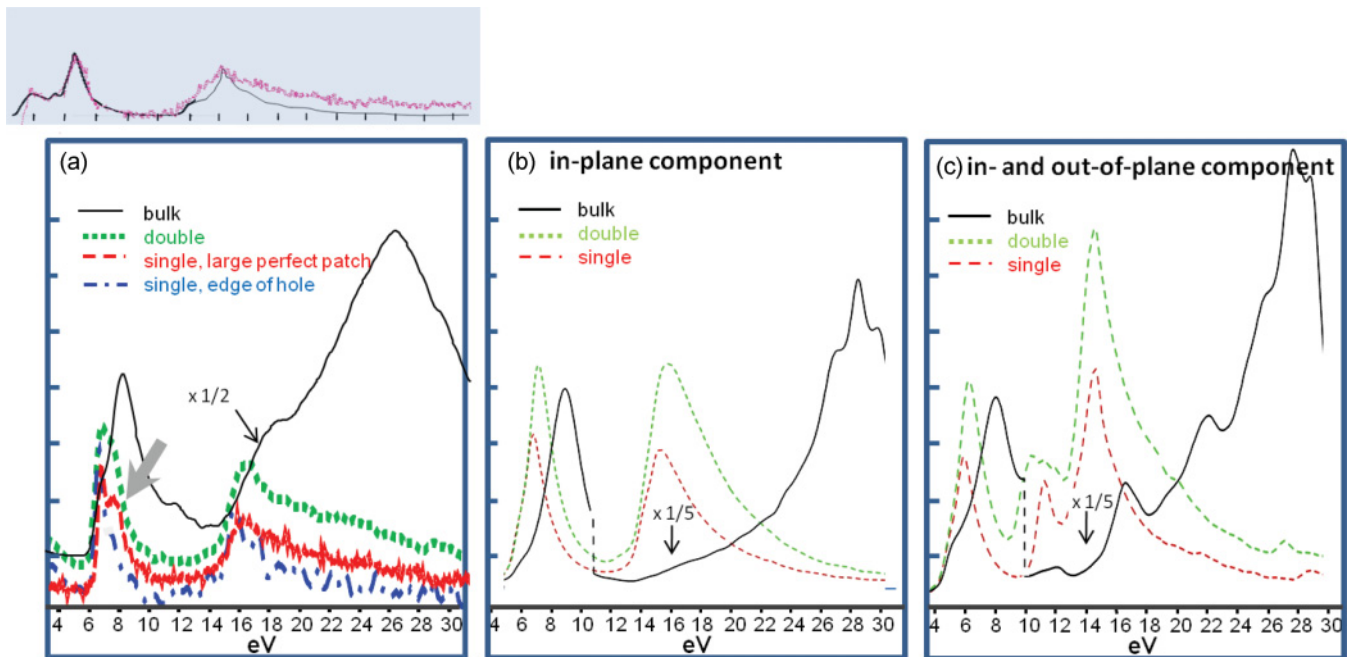

FIG. 3. (Color online) (a) Experimental, background (ZLP)-removed spectra of BN, with the electron beam penetrating bulk (solid, black), bilayer (dotted, green), and single-layer (dashed, red) BN, as well as aloof (dash-dotted, blue) to single layer perpendicular to the sheets. The 7.5-eV peak is arrowed (gray). (b) WIEN2K calculations for the in-plane plasmon component of bulk (solid, black) and double- (dashed, green) and single- (dashed, red) layer BN; (c) WIEN2K calculations for the same BN configuration as in panel b, but with an added out-of-plane plasmon component. The layer repeat distance for the separated-layer calculations is 60 Å; the number of k-points is 3000. The topmost inset shows an experimental (purple) and calculated (black) plasmon spectrum for single-layer graphene for comparison (Ref. 28). The y-axis assigns the intensity of the energy loss function in arbitrary linear units (the units size in panels b and c is the same).
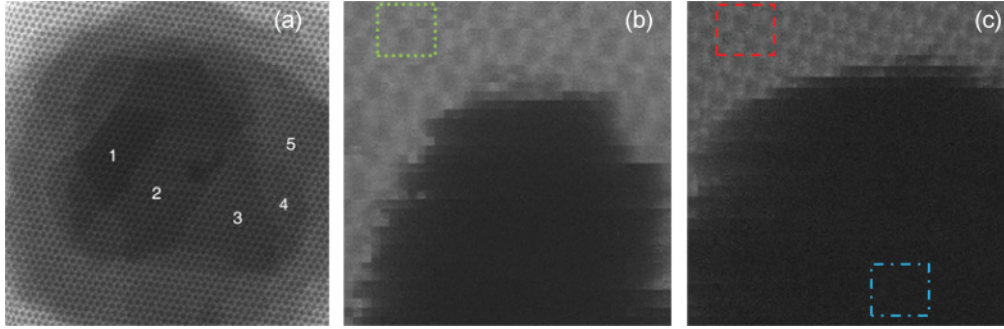
FIG. 4. (Color online) (a) HAADF image of terraces (layer numbers assigned) formed in multilayer BN as the e-beam "burns" material away; image size, 10 nm; (b) double-layer and (c) single-layer (image size, 3 nm) with hole forming during acquisition of an EEL spectrum image. The frame in panel b corresponds to the area of pixels from which the bilayer spectrum in Fig. 3(a) is taken; the frames in panel c show the areas from which the spectra of the single layer in penetrating and aloof geometry in Fig. 3(a) are extracted. Panels b and c are HAADF images acquired simultaneously with the spectrum images.

Our spectra presented in Fig. 3(a), from which the zero-loss peak (ZLP) was removed, were obtained on clean, ∼100-nm-diameter patches of single- and double-layer BN. Figures 4(b) and 4(c) shows the exact areas from which the experimental spectra in Fig. 3(a) were obtained. Prolonged e-beam exposure during acquisition of the spectrum images resulted in formation of a hole in this case, so we can compare spectra taken in penetrating and aloof e-beam configuration. Figure 4(a) shows an area of multilayer BN, which was manipulated with the e-beam to exhibit terraces of various layer numbers.

Given that EELS spectra for very thin films as well as that for single, bi-, and few-layer BN (the latter not shown here) reflect the calculated absorption spectra, although the energy peak of the plasmon increases, the rise stays the same, and hence the position of the optical band gap does not change, it can be concluded that the interlayer coupling does not affect the optical response, which is dominated by in-plane excitations.

Furthermore, experimental single-layer spectra are represented rather well by WIEN2K calculations of the in-plane component of the plasmon [compare Figs. 3(a) and 3(b)]: the calculated spectra of the out-of-plane component [Fig. 3(c)] show a pronounced peak at ∼11 eV, which is not dominant in the measured spectra. The σ- to π-plasmon intensity ratio is slightly higher in the calculated than in the measured spectra because of insufficient vacuum layer spacing, so there is still a degree of coupling between sheets. We have settled for a spacing of ∼60 Å to reduce calculation time. The peak at ∼7.5 eV decreases significantly when the plasmon is measured aloof (i.e., with the electron beam passing in the direction perpendicular to the BN sheet, but at a distance of several nanometers away from the edge [Fig. 3(a), blue dash-dotted curve]). With the beam progressing in aloof geometry near the edge of a double layer (not shown), the 7.5-eV peak is still strongly present a few nanometers away from the edge. This is arguably a further indication for the contribution of a vertical component to the 7.5-eV peak. It should be noted that the bulk BN spectra, similarly, are best represented by the in-plane component; the peak at ∼18 eV in the experimental spectrum is a surface plasmon. This is not reproduced by calculations of the 3D repeat unit cell structure, representing a bulk-only situation.

C. Influence of impurities on BN plasmon energy loss spectra

Whereas the positions of the calculated π-plasmon (∼6 eV) and σ-plasmon peak (∼14 eV) for single- and double-layer BN, and also for bulk BN (π-plasmon at ∼9 eV and σ-plasmon at ∼27 eV) are quite close to those in the experimental spectra, the latter show a much steeper rise of the π-plasmon than the single- and double- layer calculations. Conversely, the simulations of single-layer BN do not reproduce the high-energy shoulder at 7.5 eV, as observed in the experiment. Following work by Krivanek *et al.*,[29] who investigated the possibility of detecting and identifying impurity atoms in BN via atomic resolution HAADF imaging, owing to the fact that the contrast has a ∼Z^r dependency ($1.5 < r < 1.8$), and who have identified O and C impurities, we now consider the latter impurities in single-layer BN to tackle the discrepancy between simulated and experimental BN EEL spectra. We have carried out HAADF image evaluations similar to those of the above authors, and, using the relative atomic contrast as a guide, we attempted to identify O and C atoms in BN and their relative concentrations. We then used the derived relative impurity concentrations as input into the WIEN2K calculations. A systematic investigation using WIEN2K simulations will be detailed in Pan *et al.*;[21] below, we will summarize the findings that give the closest similarity with experimental data.

Intensity traces were taken parallel to the three crystallographic $\langle 11\bar{2}0 \rangle$ directions along the B-N bonds after HAADF images had been deconvolved to remove the contribution of the "tail" of the electron probe to the neighboring atoms, using the routines described in detail in Ref. 29. After background subtraction, the variation in contrast of each atomic species (N or B) was ∼±20% of the value of the respective atom. Several dozens of atomic resolution HAADF images of 5×5 nm^2 area were evaluated. Figure 6(c) shows an example of a histogram of the frequency of atoms with a certain contrast versus their HAADF intensity, extracted from a 5×5-nm^2 area. The original (raw) histogram was fitted with four Gaussian functions, whose shapes are indicated by the bars showing the redistributed numbers. The positions of the intensity maxima are in the ratio of 1:1.4:1.75:2.1, which is close to the $Z^{1.7}$ ratios for $Z = 5$ (B), $Z = 6$ (C), $Z = 7$ (N), and $Z = 8$ (O), of 1:1.4:1.77:2.23. The B profile is rather broad and askew toward

low-contrast values, giving the associated boron atom number a higher proportion than the nitrogen atom number. This is partially the case because a fraction of the nitrogen atoms has been substituted by carbon and oxygen atoms; however, the reason for the significant broadening of the boron profile is the uncertainty associated with the low-contrast values [shaded area in Fig. 6(c)]. The peak areas suggest ∼10% and ∼6% of substitutional C and O, respectively (We note that core loss spectra were also obtained, revealing a significant carbon K-edge in areas free of deposits, although signals were noisy; the signal-to-noise ratio at the higher energy losses around the oxygen K-edge was, however, too small for identification of an edge signal). Krivanek *et al.*[29] ascribe the high substitutional C and O impurity content to refilling of holes created by the e-beam in BN with atoms from the abundant hydrocarbon contamination.

Typically, 4% of the atoms showed brighter contrast, falling significantly above the +20% error margin of the N atom contrast (and also outside the tail of the N peak), lending more certainty to the assumption that they are O atoms; a 25% contrast difference is expected for N and O. About 4% of C-C bonds were recorded, with the contrast in this case falling below a −20% error margin of that of the N atoms and >20% above that of the B atoms (the expected contrast difference between N and C and between C and B atoms is ∼25%). C-C chains were furthermore identified by the similarity in the atomic contrast. Singular O atoms were recorded as well as C-O constellations. C atoms were mostly arranged in pairs, short chains, or three, four, and five atoms within six-ring structures. Figure 5(a) shows the models used to calculate EEL spectra of BN containing O only. To save computing time, the spectra here were simulated with a smaller vacuum distance, ranging from 15 to 35 Å and a lower number of k-points, around 50 to 1000. Figure 5 shows structures with one singular oxygen impurity in various-size supercells, resulting in O concentrations of ∼3% to ∼12%. The EEL spectra in Figs. 5(b) and 5(c) show that the oxygen impurities indeed introduce a shoulder in the π-plasmon at 7.5 eV. The
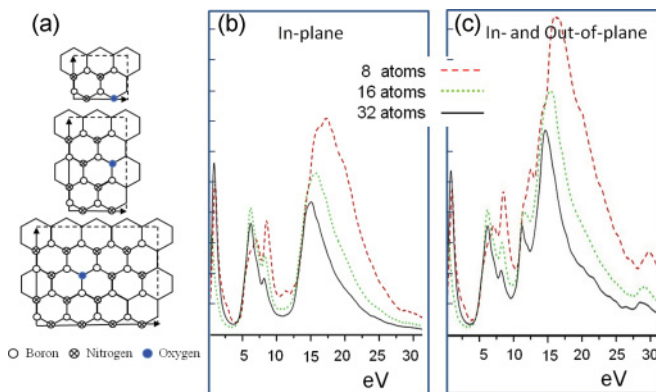

FIG. 5. (Color online) (a) Models for the WIEN2K 2D calculations used to calculate (b) the in-plane and (c) the in-plane plus out-of-plane plasmon component of single-layer BN with various amounts of oxygen. The parameters for the 8-, 16-, and 32-atom supercell calculations are 15, 25, and 35 Å vacuum layer and 1000, 500, and 100 k-points, respectively. The y-axis assigns the energy loss intensity in arbitrary, but the same, units in panels b and c.
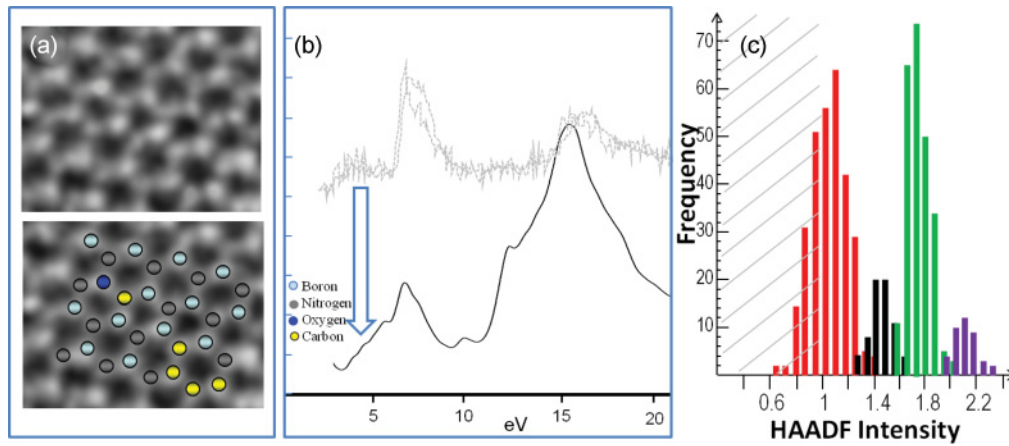
simulations for ∼3% oxygen fit the experimental spectra quite well, indicating presence of oxygen around this percentage mark, as deduced from HAADF image evaluations. The in-plane plasmon component calculation fits the experimental spectra best. Significantly, in the experimental spectra, we do not observe absorption at the rise of the π-plasmon (i.e., in the optical bandgap). Similarly, our calculated spectra show an absence of features at the rise of the π-plasmon. In their calculations Marinolpoulos *et al.*[27] find that for hBN sheets, there are no absorption features below 5 eV for the parallel, and below 10 eV for the perpendicular, component. This is unlike BN tubes, in which absorption peaks occur before the optical gap (at ∼4.5 and 5.5 eV) because of van Hove singularities or interband transitions.[30] A peak occurs at ∼1.5 eV in our calculations. However, with our energy resolution, we cannot discern such a peak in experimental spectra because of the tail of the zero-loss peak. Low-lying interband transitions (below 2 eV) would require EELS measurements with higher energy resolution. It should also be noted that although the σ-plasmon peak in our calculations is higher than the π-plasmon peak, in contrast to the experimental data, Fig. 5 shows that the σ-plasmon peak drops dramatically in intensity as the size of the vacuum layers increases. We therefore can speculate that the inconsistency in the relative plasmon peak heights results from an insufficient layer separation distance.

We have also carried out calculations for C atoms as impurities, incorporated as single atoms, as C-C "molecules" or as part of six-membered ring-type structures (details are presented in Ref. 21). These all introduce an absorption peak at the low energy side of the π-plasmon, in addition to increasing its intensity and energy. Peaks of this magnitude were not observed experimentally, whereas the observed high-energy shoulder was not produced in these calculations. In Fig. 6, we present a model structure incorporating both O and C atoms in single-layer BN. After contrast evaluation (as explained above) of, in this case, the 1.7 × 1.3-nm^2 size HAADF image in Fig. 6(a) (top), a model structure incorporating a partial carbon ring and a C-O bond [Fig. 6(a), bottom panel] was established, and WIEN2K calculations were carried out. The black-line spectrum in Fig. 6(b) corresponds to the experimentally derived structure. The calculation produces a high-energy asymmetry of the π-plasmon. It also introduces a low-energy shoulder at ∼4 eV, as seen (arrowed) in the overlaid experimental, vertically displaced spectra (gray) in Fig. 6(b). It should be noted that this preplasmon structure was only observed in a fraction of the regions investigated by EELS, and the spectra in Fig. 6(b) were not obtained from the precise area shown in Fig. 6(a). The plasmon excitation, even if created with an Å-size probe, originates from regions tens of nanometers in size, so from much larger regions than used in the supercell for the WIEN calculations in Fig. 6(b), and it is most likely that C rings, as well as C-O bonded and separate O atoms, are all present together. Hence, the model structure is not expected to replicate the experimental spectrum in detail. However, in line with further investigations (not shown here), Fig. 6 indicates that, as in the aforementioned case of C-only impurities, a preplasmon structure occurs in O-containing BN as soon as C-C bonds are added, and this structure becomes more pronounced as the C-C chain grows. When, however, oxygen is added in a configuration to form C-O bonds, the

FIG. 6. (Color online) (a) Top: 1.7×1.3-nm^2 HAADF image of single-layer BN after deconvolution with an electron probe function (Ref. 29); bottom: image with the model structure overlaid after calibration of the HAADF contrast (N: gray, B: light blue, O: dark blue, C: yellow); (b)WIEN2K calculations of EEL spectrum according to the model structure in panel a (black solid curve). A 32-atom supercell was used, including a 25-Å vacuum layer, and the k-point number was 50. Overlaid gray curve shows background (ZLP)-extracted, experimental EEL spectra; (c) histograms of B (red/dark gray), C (black), N (green/gray), and O (violet/light gray) atoms obtained from a 5×5-nm^2 area.

preplasmon peaks diminish and the postplasmon shoulder grows. Hence, it becomes clear that the plasmon shoulder at 7.5 eV is strongly influenced by O impurities. This study is to show that the experimental spectra are best reproduced by including arrangements of both, O and C impurities.

V. CONCLUSIONS

We have demonstrated the successful isolation of micrometer-sized, free-standing, single-layer BN sheets with large (of the order of 100 nm) clean areas, significantly larger than in graphene. Proof of single layers being present was obtained by electron diffraction, which also showed the distinct fingerprint of AA′ stacking in double layers. Single- and double-layer characteristics were also revealed via electron energy loss spectroscopy through the unique plasmon structure. EEL spectroscopy was accompanied by WIEN2K DFT calculations. Although the latter reproduced plasmon energies and general plasmon structure rather well, discrepancies in the detailed shape of the π-plasmon between experimental and calculated data were observed. This could only be resolved after introducing impurities into the BN sheets. Information regarding the nature and number of impurities in exfoliated BN was obtained by analyzing the atomic contrast in atomic-resolution HAADF images. This yielded percentages and positions of O and C atoms over nanoscale areas. These structures were then used to perform further WIEN2K calculations, which suggested that O impurities in BN single layers, as well as molecules including C-O and C-C bonds, introduced the experimentally observed 7.5-eV high-energy shoulder in the π-plasmon, together with preplasmon structure.

*rahul.raveendran-nair@manchester.ac.uk;
ursel.bangert@manchester.ac.uk

[1] K. S. Novoselov, D. Jiang, F. Schedin, T. J. Booth, V. V. Khotkevich, S. V. Morozov, and A. K. Geim, Proc. Natl. Acad. Sci. USA **102**, 10451 (2005).

[2] C. Lee, Q. Li, W. Kalb, X.-Z. Liu, H. Berger, R. W. Carpick, and J. Hone, Science **328**, 76 (2010).

[3] B. Radisavljevic, A. Radenovic, J. Brivio, V. Giacometti, and A. Kis, Nat. Nanotech. **6**, 147 (2011).

[4] C. Kisielowski, Q. M. Ramasse, L. P. Hansen, M. Brorson, A. Carlsson, A. M. Molenbroek, H. Topsoe, and S. Helveg, Angew. Chem., Int. Ed. **49**, 2708 (2010)

[5] L. P. Hansen, Q. M. Ramasse, C. Kisielowski, M. Brorson, E. Johnson, H. Topsoe, and S. Helveg, Angew. Chem., Int. Ed. **50**, 10153 (2011).

[6] K. Watanabe, T. Taniguchi, and H. Kanda, Nat. Mater. **3**, 404 (2004).

[7] C. R. Dean, A. F. Young, I. Meric, C. Lee, L. Wang, S. Sorgenfrei, K. Watanabe, T. Taniguchi, P. Kim, K. L. Shepard, and J. Hone, Nat. Nanotech. **5**, 722 (2010).

[8] A. S. Mayorov, R. V. Gorbachev, S. V. Morozov, L. Britnell, R. Jalil, L. A. Ponomarenko, P. Blake, K. S. Novoselov, K. Watanabe, T. Taniguchi, and A. K. Geim, Nano Lett. **11**, 2396 (2011).

[9] J. C. Meyer, A. Chuvilin, G. Algara-Siller, J. Biskupek, and U. Kaiser, Nano Lett. **9**, 2683 (2009).

[10] W.-Q. Han, L. Wu, Y. Zhu, K. Watanabe, and T. Taniguchi, Appl. Phys. Lett. **93**, 223103 (2008).

[11] R. V. Gorbachev, I. Riaz, R. R. Nair, R. Jalil, L. Britnell, B. D. Belle, E. W. Hill, K. S. Novoselov, K. Watanabe, T. Taniguchi, A. K. Geim, and P. Blake, Small **7**, 465 (2011).

[12] C. Jin, F. Lin, K. Suenaga, and S. Iijima, Phys. Rev. Lett. **102**, 195505 (2009).

[13]N. Alem, R. Erni, C. Kisielowski, M. D. Rossell, W. Gannett, and A. Zettl, Phys. Rev. B **80**, 155425 (2009).

[14]T. Eberlein, U. Bangert, R. R. Nair, R. Jones, M. Gass, A. L. Bleloch, K. S. Novoselov, A. Geim, and P. R. Briddon, Phys. Rev. B **77**, 233406 (2008).

[15]R. R. Nair, P. Blake, J. R. Blake, R. Zan, S. Anissimova, U. Bangert, A. P. Golovanov, S. V. Morozov, A. K. Geim, K. S. Novoselov, and T. Latychevskaia, Appl. Phys. Lett. **97**, 153102 (2010).

[16]T. Taniguchi and K. Watanabe, J. Cryst. Growth **303**, 525 (2007).

[17]T. J. Booth, P. Blake, R. R. Nair, D. Jiang, E. W. Hill, U. Bangert, A. Bleloch, M. Gass, K. S. Novoselov, M. I. Katsnelson, and A. K. Geim, Nano Lett. **8**, 2442 (2008).

[18]O. L. Krivanek, G. J. Corbin, N. Dellby, B. F. Elston, R. J. Keyse, M. F. Murfitt, C. S. Own, Z. S. Szilagyi, and J. W. Woodruff, Ultramicroscopy **108**, 179 (2008).

[19]P. Blaha, K. Schwarz, G. K. Madsen, D. Kasnicka and J. Luitz, *Wien2k, An Augmented Plane Wave + Local Orbitals Program for Calculating Crystal Properties* (Karlheinz Schwarz, Techn. Universität Wien, Austria, 2001).

[20]C. A. Draxl and J. O. Sofo, Comput. Phys. Commun. **175**, 1 (2006).

[21]C.-T. Pan, C. Seabourne, A. J. Scott *et al.* (to be published)

[22]R. J. Nicholls and A. J. Scott, J. Phys.: Conf. Ser. **126**, 012038 (2008).

[23]C. R. Seabourne, A. J. Scott, R. Brydson, and R. J. Nicholls, Ultramicroscopy **109**, 1374 (2009).

[24]J. C. Meyer, A. K. Geim, M. I. Katsnelson, K. S. Novoselov, T. J. Booth, and S. Roth, Nature **446**, 60 (2007).

[25]J. C. Meyer, A. K. Geim, M. I. Katsnelson, K. S. Novoselov, D. Obergfell, S. Roth, C. Girit, and A. Zettl, Solid State Commun. **143**, 101 (2007).

[26]R. Arenal, O. Stephan, M. Kociak, D. Taverna, A. Loiseau, and C. Colliex, Phys. Rev. Lett. **95**, 127601 (2005).

[27]A. G. Marinopoulos, L. Wirtz, A. Marini, V. Olevano, A. Rubio, and L. Reining, Appl. Phys. A **78**, 1157 (2004).

[28]U. Bangert, C. T. Pan, R. R. Nair, and M. H. Gass, Appl. Phys. Lett. **97**, 253118 (2010).

[29]O. L. Krivanek, M. F. Chisholm, V. Nicolosi, T. J. Pennycook, G. J. Corbin, N. Dellby, M. F. Murfitt, C. S. Own, Z. S. Szilagyi, M. P. Oxley, S. T. Pantelides, and S. J. Pennycook, Nature **464**, 571 (2010).

[30]J. S. Lauret, R. Arenal, F. Ducastelle, A. Loiseau, M. Cau, B. Attal-Tretout, E. Rosencher, and L. Goux-Capes, Phys. Rev. Lett. **94**, 037405 (2005).